ACS APPLIED ELECTRONIC MATERIALS

pubs.acs.org/acsaelm Article

Tuning the Electronic and Mechanical Properties of Two-Dimensional Diamond through N and B Doping

Bruno Ipaves,* João F. Justo, Biplab Sanyal, and Lucy V. C. Assali

Cite This: ACS Appl. Electron. Mater. 2024, 6, 386−393 Read Online

ACCESS | Metrics & More | Article Recommendations

ABSTRACT: This paper examines the structural, thermodynamic, dynamic, elastic, and electronic properties of doped 2D diamond C_4X_2 (X = B or N) nanosheets in both AA′A″ and ABC stacking configurations, by first-principles calculations. Those systems consist of three diamond-like graphene sheets with an undoped graphene layer between two 50% doped ones. Our results, based on the analysis of ab initio molecular dynamics simulations, phonon dispersion spectra, and Born's criteria for mechanical stability, revealed that all four structures are stable. Additionally, their standard enthalpy of formation values are similar to that of pristine 2D diamonds, recently synthesized by compressing three graphene layers together. The C_4X_2 (X = B or N) systems exhibit high elastic constant values and stiffness comparable to that of bulk diamond. The C_4N_2 nanosheets present wide indirect band gaps that could be advantageous for applications similar to those of the hexagonal boron nitride (h-BN), such as a substrate for high-mobility 2D devices. On the other hand, the C_4B_2 systems are semiconductors with direct band gaps, in the 1.6−2.0 eV range, and small effective masses, which are favorable characteristics to high carrier mobility and optoelectronics applications.

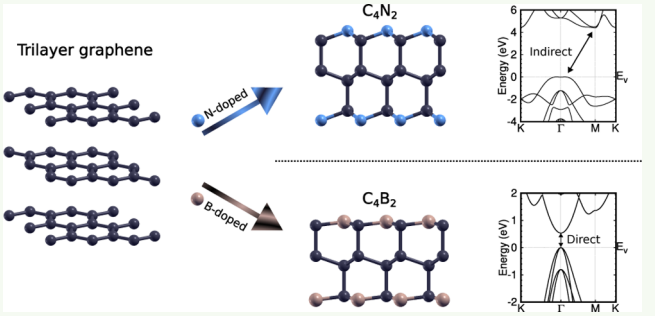

KEYWORDS: *2D diamond, diamane, ultrathin diamond films, functionalization, DFT, first-principles calculations*

INTRODUCTION

Graphene is the most popular two-dimensional (2D) material, being a zero-gap semimetal with a honeycomb carbon structure and sp^2 hybridization. It carries a unique combination of physical properties in nature such as high electrical conductivity, tensile strength, and optical transparency. Additionally, it is the elementary structure for several other nanomaterials, such as fullerenes, nanotubes, graphite, and the single-layer diamond (2D diamond).[1−3] As a result of recent developments in the synthesis and characterization of 2D materials, the 2D diamond has received great attention, with promising applications in several fields, such as batteries, quantum computing, nano-optics, and nanoelectronics.[4]

The stabilization of 2D diamond often requires surface functionalization, leading to a variety of structures, which have received different labels, such as diamane, diamene, diamondol, and diamondene.[4,5] 2D diamonds can also be built out of bilayer graphene or few-layer graphene (FLG) through different techniques. For example, the two-layer hydrogenated (HD) and fluorinated (FD) 2D diamonds can be synthesized at ambient pressure without a substrate, in which the HD can be produced using hot filament chemical vapor deposition,[6] while FD by combining FLG and gaseous ClF_3.[7] However, films with three layers or more face a nucleation barrier that increases with the number of layers, requiring pressure assistance.[8]

The pristine 2D diamond (PD) is hard to synthesize as high pressures are required to transform sp^2 bonds from graphene layers into interlayer sp^3 ones.[5] Recently, PD has been synthesized without a substrate by compressing three layers of graphene.[9] However, it reverts to graphene when the pressure is released, in agreement with a previous theoretical study.[10] Furthermore, theoretical investigations have demonstrated the potential for stabilizing 2D diamond structures, composed of two graphene layers, through nitrogen substitution.[11] The NCCN 2D structure, composed of two carbon layers functionalized with nitrogen on both sides, has been explored by various research groups,[12−14] suggesting its potential application as a selective ammonia sensor.[13]

The physical properties of 2D diamonds may vary considerably, depending on the synthesis methods, leading to structures with different configurations, functional groups, and heteroatoms.[4,5] For example, B and N dopants can tune the electronic properties, as well as enhance stability and reduce the

Received: October 6, 2023
Revised: December 15, 2023
Accepted: December 18, 2023
Published: January 4, 2024

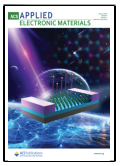

formation energy of 2D diamonds, thereby promoting their synthesis.[15−17] At room temperature, the thermal conductivity of HD is high, and the heat transport arises from the acoustic phonon modes. On the other hand, under the same conditions, the thermal conductivity of FD is lower than that of HD and the heat transport is controlled by the optical phonon modes.[18] 2D diamonds also present remarkable mechanical properties, with stiffness and Young's modulus similar to the ones of graphene and bulk diamond.[19] Furthermore, unlike graphene, 2D diamonds have band gap features that depend on the stacking arrangement, the number of layers, and the functional groups present in the structures.[4,20] Despite several recent experimental and theoretical investigations on 2D diamonds, the origin of all these peculiar properties has been the subject of debate.[4,5]

In this letter, we present a study of the physical properties of 2D diamonds doped with substitutional N or B atoms. The reference systems consist of three graphene sheets: an undoped graphene layer between two 50% doped ones, where the C−C bonds between neighboring layers are strong covalent bonds. Here, we considered four structure configurations labeled AA′A″-C_4N_2, ABC-C_4N_2, AA′A″-C_4B_2, and ABC-C_4B_2. Their structural, thermodynamic, dynamic, elastic, and electronic properties and potential applications are explored and discussed in depth.

COMPUTATIONAL METHODS

This investigation was performed using first-principles calculations based on the Density Functional Theory (DFT),[21,22] using the plane-wave basis set and projector augmented-wave (PAW) method,[23] as implemented in the Quantum ESPRESSO computational package.[24,25] We utilized the generalized gradient approximation of Perdew−Burke−Ernzerhof (GGA-PBE) exchange−correlation functional[26] and the Dion et al. scheme[27] optimized by Klimeš et al. (optB88-vdW[28]) to properly describe the effects of the dispersive van der Waals (vdW) interactions. For an accurate description of the energy band gap values, we employed the hybrid Heyd−Scuseria−Ernzerhof (HSE) functional[29] at the relaxed structures obtained from the optB88-vdW approximation. The plane-wave energy cutoff was set to 1100 eV with a convergence threshold of 0.1 meV/atom for the total energy. We used a 16 × 16 × 1 k-point mesh to describe the irreducible Brillouin zone,[30] and the forces on atoms were converged down to 1 meV/Å. To obtain the phonon dispersion curves, we used the density functional perturbation theory[31] with an 8 × 8 × 1 q-point mesh.

The primitive hexagonal cells of the 2D structures were constructed using six atoms. To determine the cell parameters in the xy-plane, variable cell optimization was carried out with the BFGS quasi-newton algorithm. In order to avoid interactions among cell images, the lattice parameter perpendicular to the sheets (z-axis) was fixed at 25 Å. This approach has been successfully applied to similar 2D systems in previous studies.[12,32,33]

In order to determine the elastic properties of the systems, we built a rectangular cell with 12 atoms and used the strain−energy method.[34,35] Accordingly, for isotropic structures and small deformations (ϵ) near their equilibrium configurations, the elastic energy, per unit area, was approximated as

$$E(\epsilon) - E(0) \approx \frac{1}{2}E^{(2)}\epsilon^2 \quad (1)$$

where $E(\epsilon)$ is the total energy of strained configurations, while $E(0)$ is the total energy of the respective unstrained ones. We applied two in-plane deformations, ranging from −1.2 to 1.2%, in order to obtain the $E^{(2)}$, which allowed us to obtain the elastic constants after fitting a second-order polynomial to the data. Herein, $E^{(2)} = C_{11}$ elastic constant for the zigzag axial deformation, while $E^{(2)} = 2(C_{11} + C_{12})$ for the biaxial planar deformation.[34,35]

The thermal stability was studied by computing the standard enthalpy of formation, per atom, of the structures at 0 GPa (ΔH_f^0), by using

$$\Delta H_f^0 = \frac{E_t(C_4X_2) - 4E_t(C) - 2E_t(X)}{6} \quad (2)$$

where $E_t(C_4X_2)$ is the total energy of the 2D nanosheet, with 4C atoms and 2X atoms (X = B or N) in the primitive cell. $E_t(C)$ and $E_t(X)$ are the total energies, per atom, of the respective C and X standard ground states, i.e., of graphite and the crystalline boron in the trigonal structure (β-boron) or the isolated N_2 molecule. This procedure to determine enthalpies and/or energies of formation has been successfully used to investigate several other systems.[36−40]

Additionally, ab initio molecular dynamics simulations (AIMD) were carried out using the Vienna ab initio simulation package (VASP),[41] in which a 6 × 6 × 1 hexagonal 216-atom supercell was adopted to allow for possible structural reconstructions. A Nose−Hoover thermostat (NVT) ensemble was employed at 300, 500 and 1000 K for 5 ps, with a simulation time step of 1 fs.

RESULTS AND DISCUSSION

Initially, we explored the physical properties of PD in AA′A″ and ABC stacking structural configurations, composed of three graphene layers in which the C atoms between layers are covalently bonded with a near sp^3 hybridization. Starting the simulations with the diamond-like configuration, they converged, after the relaxation of atomic positions, to trilayer graphene systems with vdW interactions between layers (graphite-like). This behavior has also been found in a previous theoretical investigation of 2D diamond, starting the simulations with two graphene layers.[42] These results can be understood as a consequence of the absence of an external pressure-induced and/or surface passivation to promote the sp^2 to sp^3 hybridization transformation.[42] Those pristine structures represent the reference systems used here to study and understand the effects of their functionalization.

Then, we explored the properties of C_4X_2 (X = B or N) systems, which can be described as three graphene sheets in which four C atoms are bonded covalently (2D diamond-like) in each unit cell. The two external layers are 50% doped with substitutional X atoms; hence, each X atom is bonded to three C atoms. Figure 1 presents a schematic representation of the optimized and relaxed C_4X_2 (X = B or N) systems, in both AA′A″ and ABC stacking configurations, as well as the respective labels given to the intraplanar bond angle (θ), intralayer (d_{C-X}) and interlayer (h_{C-C}) distances, and systems' thickness (Δh).

The optimized structural parameters of C_4X_2 (X = B or N) nanosheets are shown in Table 1, where the distance labels are consistent with the ones defined in Figure 1. It can be observed that all of the nanosystems functionalized with N atoms keep the lattice constants almost unchanged when compared to the PD ones. Additionally, for both stacking configurations of the C_4N_2, the intraplanar bond angle (θ) values are close to the sp^3 hybridization ones (109.47°), leading to a thickness of ≈4.7 Å. Nevertheless, the C_4B_2 nanosheet lattice parameters are slightly greater than those of HD and FD systems, with θ close to the value of 120°, i.e., the B atoms bonded to three adjacent C atoms present a sp^2-type hybridization and hence we observed a smaller thickness of ≈4.2 Å as compared to the N-functionalized structures.

We now discuss the stability of the C_4X_2 nanosheets. To study the thermal stability of those structures, we computed the standard enthalpy of formation ΔH_f^0 using eq 2. Herein, we

https://doi.org/10.1021/acsaelm.3c01398
ACS Appl. Electron. Mater. 2024, 6, 386−393

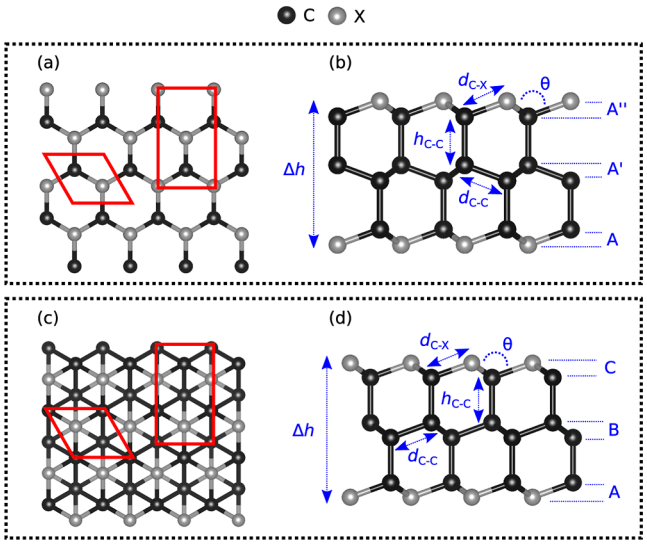

Figure 1. Schematic illustration of the C_4X_2 (X = B or N) systems. (a) Top and (b) side views of AA′A″-C_4X_2, (c) top and (d) side views of ABC-C_4X_2. The black and gray spheres represent the C and X atoms, respectively. The red lines denote the simulation unit cell limits with the rectangle cells used to determine the elastic properties. The graphs also indicate the labels given to the intralayer (d_{C-X}) and interlayer (h_{C-C}) distances, structure thickness (Δh), and the intraplanar bond angle (θ).

found positive ΔH_f^0 values of 424, 365, 348, and 333 meV for AA′A″-C_4B_2, ABC-C_4B_2, AA′A″-C_4N_2, and ABC-C_4N_2, respectively, as displayed in Table 1, indicating possible thermodynamic instability. However, the literature has reported 2D materials synthesized by endothermic processes ($\Delta H_f^0 > 0$), such as graphene, germanene, and silicene.[35,39] Also, the ΔH_f^0 values of C_4X_2 nanosheets are similar to the 300 meV/atom of PD with three graphene layers at 0 GPa (Table 1), which was recently synthesized,[9] and slightly higher than NCCN that was theoretically studied to stabilize the 2D diamond without any passivation.[11]

The thermodynamic stability of the systems was also investigated by AIMD simulations. The results exhibited a small total energy variation over 5 ps at 300 K, as shown in Figure 2, indicating that the structural integrity of those systems is maintained at those conditions. At 1000 K, the same behavior is observed for the C_4N_2 systems, while the C_4B_2 nanosheets presented some broken bonds, suggesting some structural degradation. We also performed AIMD at 500 K for the C_4B_2 nanosheets, and the structures maintained their integrity. Consequently, we project the stability of C_4B_2 systems at temperatures exceeding 500 K but remaining below 1000 K. The findings suggest stability for all systems, particularly at room temperature, with C_4N_2 nanosheets exhibiting superior thermal stability compared to C_4B_2. Nevertheless, further investigations are warranted to explore the equilibrium behavior of the system's average total energy about temperature. These studies aim to delineate the temperature threshold at which the system can sustain its structural integrity.

Furthermore, the dynamic stability of the systems was investigated by using the phonon theory, in which a system is considered stable when its vibrational spectrum contains only positive frequencies. Figure 3 presents the phonon dispersion curves of C_4B_2 and C_4N_2 compounds, in both AA′A″ and ABC stacking configurations. All spectra show 18 phonon branches, related to the six atoms present in the primitive cell. All of those systems are dynamically stable since there are only positive frequencies.

Next, we computed the elastic constants of the systems using eq 1 to verify their mechanical stability, according to the Born stability criteria ($C_{11} > 0$ and $C_{12} < C_{11}$).[43] Table 2 presents the elastic constants C_{11}, C_{12}, and $C_{66} = (C_{11} - C_{12})/2$, Young's modulus $Y^{2D} = (C_{11}^2 - C_{12}^2)/C_{11}$, and the Poisson ratio $\nu = C_{12}/C_{11}$ of C_4X_2 trilayers (X = B or N), as well as those of several other 2D materials for comparison.

Accordingly, the C_4X_2 structures are mechanically stable since they satisfy the Born criteria, agreeing with the phonon dispersion spectra shown in Figure 3. The C_4X_2 exhibits a high Young's modulus and Poisson ratio (σ) values below 0.5. 2D materials possessing Poisson's ratios between 0 and 0.5 undergo contraction in the transverse direction when stretched longitudinally. However, specific monolayers with low symmetry demonstrate a negative Poisson's ratio or auxetic behavior.[47,48]

Additionally, we estimated the longitudinal and transversal acoustic velocities for in-plane modes based on the phonon spectra (Figure 3) and also through the following equation

$$v_{LA} = \left(\frac{C_{11}}{\rho_{2D}}\right)^{1/2} \text{ and } v_{TA} = \left(\frac{C_{66}}{\rho_{2D}}\right)^{1/2} \quad (3)$$

where ρ_{2D} is the formal density, allowing comparison among systems, independent of their thickness.[4] The velocity values, as listed in Table 2, suggest that the stiffness of the C_4X_2 systems is comparable to that of the diamond.

Table 1. Structural Properties of C_4X_2 (X = B or N): Lattice Parameter (a), Intralayer (d) and Interlayer (h) Distances, Thickness (Δh), and Intraplanar Bond Angle (θ), Labeled According to Figure 1[a]

system	a	d_{C-X}	d_{C-C}	h_{C-C}	Δh	θ	ΔH_f^0
AA′A″-C_4N_2	2.42	1.49	1.49	1.60	4.74	108.9	348
ABC-C_4N_2	2.44	1.50	1.50	1.57	4.66	109.0	333
AA′A″-C_4B_2	2.66	1.55	1.62	1.66	4.25	118.4	424
ABC-C_4B_2	2.67	1.55	1.63	1.65	4.18	118.5	365
3-layers PD[b]	2.43	Y[b]	1.54	1.65		Y[b]	300
2-layers HD[20]	2.53	1.56		1.56			
2-layers FD[20]	2.56	1.55		1.55			
2-layers NCCN	2.39[12]	1.47[12]		1.58[12]	2.59[11]	108.8[12]	211[11]

[a]The distances are given in Å and the angles in degrees. The standard enthalpies of formation (ΔH_f^0) at 0 pressure are given in meV/atom. For PD, HD, and FD, X = C. [b]($\bar{2}110$)-oriented h-diamane exhibits two d_{C-X} and θ values. Y = bond lengths are 1.35 and 1.54 Å with the angles presenting sp^3 and sp^2 hybridization.[9]

https://doi.org/10.1021/acsaelm.3c01398
ACS Appl. Electron. Mater. 2024, 6, 386−393

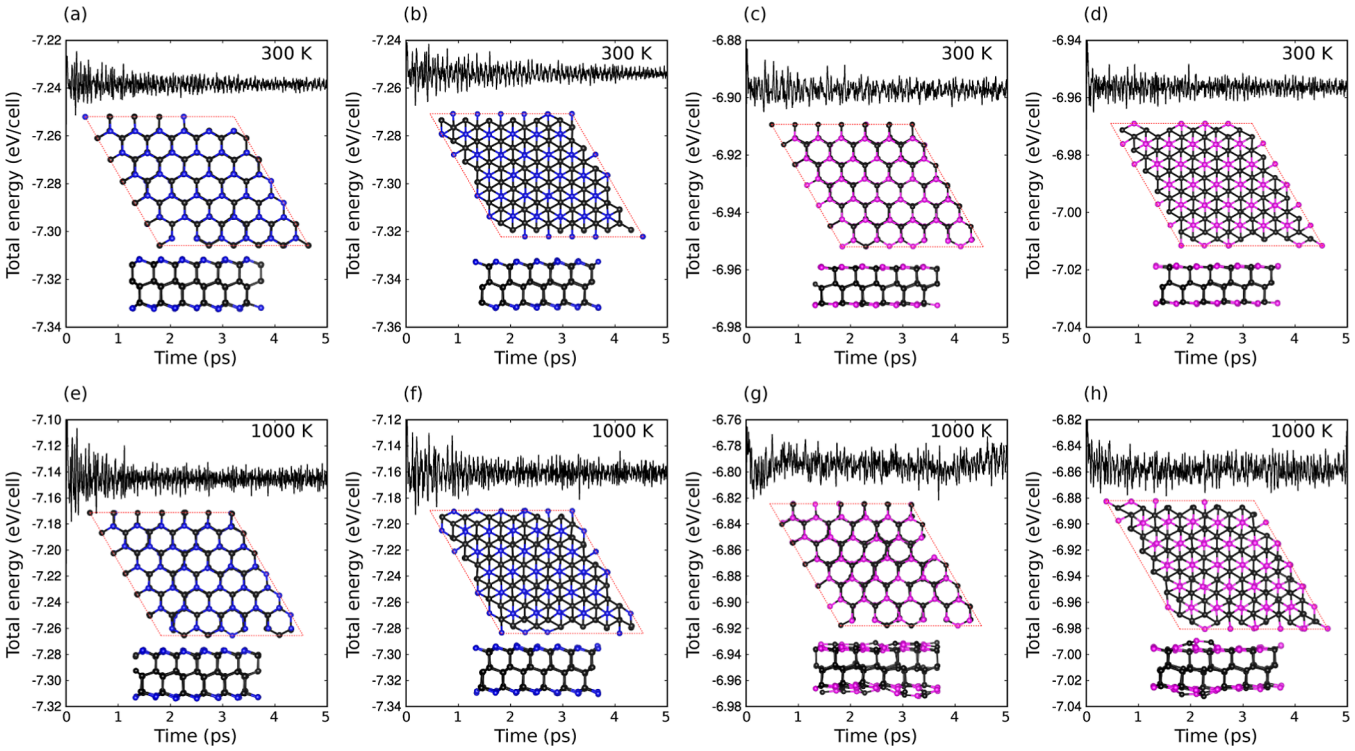

Figure 2. Systems' total energy variation during 5 ps, computed with AIMD simulations. At 300 K, the results are (a) AA′A″-C_4N_2, (b) ABC-C_4N_2, (c) AA′A″-C_4B_2, and (d) ABC-C_4B_2. At 1000 K, results of (e) AA′A″-C_4N_2, (f) ABC-C_4N_2, (g) AA′A″-C_4B_2, and (h) ABC-C_4B_2.

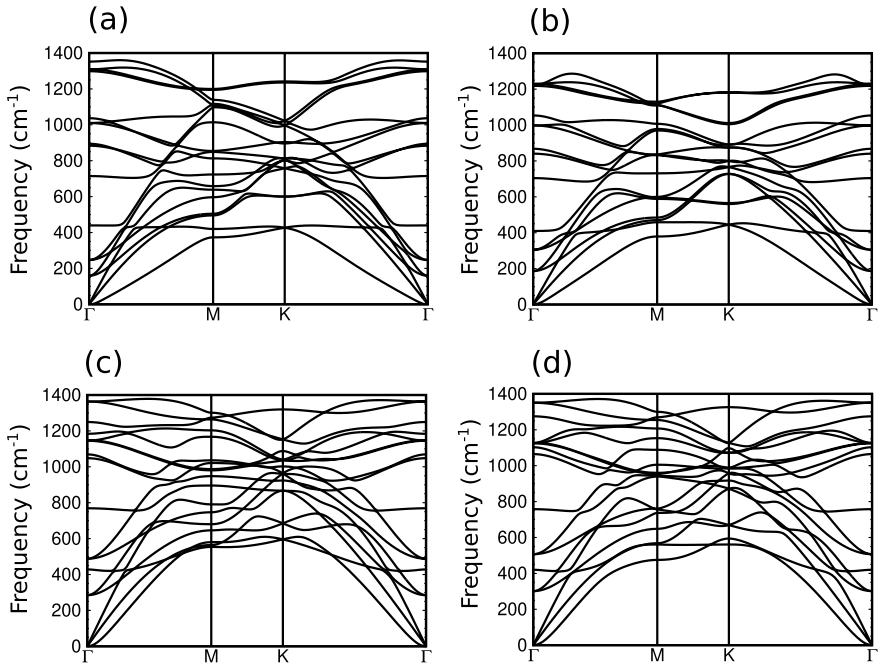

Figure 3. Phonon dispersion branches of (a) AA′A″-C_4B_2, (b) ABC-C_4B_2, (c) AA′A″-C_4N_2, and (d) ABC-C_4N_2 along the main high-symmetry directions in the BZ of the hexagonal lattice.

Subsequently, we studied the electronic band structures and the projected density of states (PDOS) of the C_4X_2 systems, as displayed in Figure 4a−d. The electronic band structures and PDOS of AA′A″-C_4N_2 and ABC-C_4N_2 nanosheets, as presented in Figure 4a,b, exhibit some differences, despite their analogous PDOS, showing that the N p-orbitals dominate at the valence band maximum (VBM) while the conduction band minimum (CBM) are mostly characterized by a mixture of s- and p-orbitals of N and C atoms. Both systems present the VBM around the Γ-point with a Mexican-hat dispersion, in which the two peaks lie on the Γ−*K* and Γ−*M* lines. The height of the Mexican-hat-type dispersion band at the Γ-point is 0.01 and 0.001 eV for AA′A″-C_4N_2 and ABC-C_4N_2 nanosheets, respectively. However, the CBM of ABC-C_4N_2 is well-defined at the *M*-valley, while in AA′A″-C_4N_2 although the CBM is located at the *M*-valley, the energy of the *K*-point is very close to the *M*-point. On the other

https://doi.org/10.1021/acsaelm.3c01398
ACS Appl. Electron. Mater. 2024, 6, 386−393

Table 2. Elastic Constants C_{11}, C_{12}, and C_{66}, Young's Modulus Y^{2D}, Poisson Ratio σ, Formal Density ρ_{2D}, Longitudinal v_{LA} and Transverse v_{TA} Acoustic Velocities of C_4X_2 (X = B or N), Graphene, and Other 2D Diamonds[a]

system	C_{11}	C_{12}	C_{66}	Y^{2D}	σ	ρ_{2D}	v_{LA}	v_{TA}
AA′A″-C_4N_2	816	85	366	808	0.10	24.8	18.1 (18.1)	12.1 (12.1)
ABC-C_4N_2	777	82	348	769	0.11	24.5	17.8 (17.6)	11.9 (11.8)
AA′A″-C_4B_2	627	88	270	615	0.14	18.9	18.2 (16.4)	11.9 (10.8)
ABC-C_4B_2	609	92	259	595	0.15	18.7	18.0 (16.1)	11.7 (10.6)
graphene	354[34]	60[34]	147*	340[44]	0.18[45]	7.55[45]	21.6*	13.9*
2-layers HD[45]	474	36	219*	471*	0.08	14.9	17.8	12.2
2-layers FD	485[20]	50[46]	218*	480[20]	0.10*		14.0[4]	9.3[4]
2-layers NCCN[11]	568	66	243	560*	0.12*			
3-layers HD[45]	718	58	330*	713*	0.08	22.2	18.0	12.2
3-layers FD[46]	∼700	∼70	315*	693*	0.10*		15.0	10.0
diamond	1079[11]	124[11]	578[11]				18.3[45]	12.4[45]

[a]Elastic constants and Young's modulus are given in N/m, Poisson ratio is dimensionless, formal density and velocities are given in 10^{-7} kg/m^2 and km/s, respectively. The bulk diamond elastic constants are given in GPa. The acoustic velocities were estimated through two distinct methods: utilizing eq 3 and extracting information from the phonon spectra illustrated in Figure 3 (within parentheses). The results with the * symbols were obtained using the literature data from this table and the equations described in this paper.

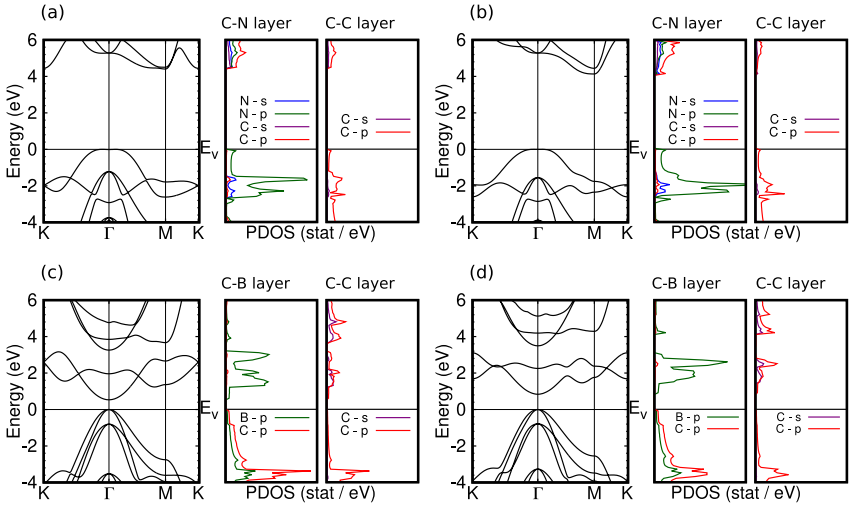

Figure 4. Electronic band structures along the main high-symmetry directions of the BZ and PDOS, obtained with the optB88-vdW approach for the exchange−correlation energy: (a) AA′A″-C_4N_2, (b) ABC-C_4N_2, (c) AA′A″-C_4B_2, and (d) ABC-C_4B_2. The PDOS on the C and X s-orbitals are given in purple and blue, respectively, and those on the C and X p-orbitals are given in red and green, respectively. E_v represents the VBM. Energies and PDOS are given in eV and states/eV, respectively.

Table 3. Electronic Band Gap Width of C_4X_2 (X = B or N) Nanosheets (in eV), Obtained with Two Different Approximations for the Exchange−Correlation Functional: optB88-vdW[28] (E_g^{vdW}) and HSE[29] (E_g^{HSE})[a]

system	E_g^{vdW}	E_g^{PBE}	E_g^{HSE}	band gap	m_h*	m_e*	$m_e^{*M\to\Gamma}$	$m_e^{*M\to K}$
AA′A″-C_4N_2	4.40		5.56	indirect	6.23		2.94	0.30
ABC-C_4N_2	4.13		5.42	indirect	16.77		2.61	0.47
AA′A″-C_4B_2	0.53		1.64	direct	0.34 (0.68)	1.22		
ABC-C_4B_2	0.84		1.97	direct	0.36 (0.80)	1.30		
2-layers HD[20]		3.32		direct	0.21 (0.58)	1.11		
2-layers FD[20]		4.04		direct	0.37 (1.13)	0.55		
3-layers PD[9]			2.70	indirect				

[a]The bandwidth of $(\bar{2}110)$-oriented h-diamane with three graphene layers is also presented for PD. The electron (m_e*) and hole (m_h*) effective masses, in m_0 units, obtained with the optB88-vdW approach are also shown. The VBM of C_4B_2 systems is doubly degenerated at the Γ-point and has two values for hole carriers: the light hole effective mass and the heavy hole effective mass (in parentheses). The CBM of C_4N_2 systems displays two effective masses around the M-valley, $m_e^{*M\to\Gamma}$ and $m_e^{*M\to K}$.

hand, the AA′A″-C_4B_2 and ABC-C_4B_2 nanosheets have very similar band structures, as shown in Figure 4c,d. Both systems present direct band gaps, where the doubly degenerated VBM and the CBM are located at the Γ-point in which the B p-orbitals dominate at the CBM and the VBM is described by a combination of B and C p-orbitals.

As discussed in the Introduction section, the 2D diamond systems present nonzero band gaps with characteristics that depend on several factors, such as doping with different

https://doi.org/10.1021/acsaelm.3c01398
ACS Appl. Electron. Mater. 2024, 6, 386−393

Table 4. Summary of the Qualitative Properties and Potential Applications of C_4X_2 (X = B and N) Systems[a]

system	DS	MS	TS (300 K)	TS (1000 K)	Y^{2D}	stiffness	band gap	m^*	potential applications
C_4N_2	yes	yes	yes	yes	high	high	indirect	heavier	host material for single-photon emission/quantum computing biosensors
C_4B_2	yes	yes	yes	no	high	high	direct	lighter	nano-optics nanoelectronics

[a]The columns indicate dynamic (DS), mechanic (MS), and thermodynamic (TS) stability, Young's modulus Y^{2D}, and effective masses (m^*).

functional groups. Herein, we are working with B and N atoms as X-doping elements, in which the B atom belongs to group-III elements of the periodic table, with a $2s^2 2p^1$ valence electronic configuration, and the N atom belongs to group-V elements, with a $2s^2 2p^3$ valence electronic configuration. As a result, we found a wider indirect band gap for the C_4N_2 nanosheets and a narrower direct band gap for the C_4B_2 systems when compared to PD. Table 3 displays the band gap values of the C_4X_2 nanosheets obtained with the optB88-vdW[28] (E_g^{vdW}) and the hybrid HSE[29] (E_g^{HSE}) functional approaches for the exchange−correlation energy. For comparison, we also included the HD and FD band gap values acquired with PBE functional[20] and of the three-layer graphene PD obtained with hybrid HSE functional.[9] The band gap width of the latter is 2.70 eV, while for the AA′A″-C_4N_2, ABC-C_4N_2, AA′A″-C_4B_2, and ABC-C_4B_2-functionalized compounds, they are 5.56, 5.42, 1.64, and 1.97 eV, respectively, using the same exchange−correlation potential. The C_4N_2 nanosheets have band gap width values, obtained with the optB88-vdW approach, similar to those obtained with the PBE approximation for the HD and FD systems.

Furthermore, since effective masses (m^*) can be used to investigate electronic transport under the influence of electric fields or carrier gradients, we estimated them by fitting parabolic functions to the CBM and VBM via the formula as follows

$$\frac{1}{m^*} = \frac{1}{\hbar^2}\left|\frac{\partial^2 E(k)}{\partial k^2}\right| \tag{4}$$

where $E(k)$ and k are the energy and the wave vector of the CBM or VBM. The values of the effective masses depend on the curvature radius of the electronic band around the band-edge position, i.e., a larger curvature radius implies a heavier carrier effective mass.

The electron (m_e^*) and hole (m_h^*) effective masses, in m_0 units, calculated with the optB88-vdW approach, are presented in Table 3. In both stacking structures of the C_4B_2 nanosheets, the VBM is doubly degenerate at the Γ-point, exhibiting two values for hole carriers: a light hole effective mass $m_{lh}^* = 0.34m_0$ and a heavy hole effective mass $m_{hh}^* = 0.68m_0$ for the AA′A″ configuration, and $m_{lh}^* = 0.36m_0$ and $m_{hh}^* = 0.80m_0$ for the ABC configuration. Additionally, we determined electron effective masses of $m_e^* = 1.22m_0$ and $m_e^* = 1.30m_0$ for AA′A″ and ABC stacking, respectively. The electrons and holes effective masses are comparable to the ones of HD and FD systems, which present extraordinary carriers mobility.[20] Furthermore, these estimated effective masses are similar to the $m_e^* = 1.06m_0$ and $m_h^* = 0.59m_0$ of silicon at a temperature of 4 K.[49] Regarding C_4N_2 nanosheets, the m_h^* is the magnitude of the effective mass at Γ-point, i.e., we fitted a parabolic function considering the minimum located at the Γ-point.[50] Accordingly, the m_h^* depends on the height of the Mexican-hat-type dispersion band and the radius centered at Γ-point around band edges.[50] On the other hand, electrons in the CBM display two distinct effective mass values around the M-valley, depending on the high symmetry line chosen from the M-point. The $m_e^{*M\to\Gamma}$ is a great electron effective mass, much greater than $m_e^{*M\to K}$: $m_e^{*M\to\Gamma}$ is five times greater than $m_e^{*M\to K}$ for ABC-C_4N_2 and nine times greater for AA′A″-C_4N_2.

Considering the stable structures presented previously and their physical properties, it is interesting to explore their potential applications. Further investigations could explore the applicability of C_4N_2 and C_4B_2 structures as building blocks to build 2D/3D systems, such as vdW heterostructures, with different properties.[12,51,52] Moreover, wide band gap materials, such as hexagonal boron nitride (h-BN), serve as a substrate for high-mobility 2D devices,[53] a host material for single-photon emitter defect-centers for quantum computing and biosensors,[4] etc. Therefore, the C_4N_2 nanosheets seem appropriate for these kinds of applications. Finally, the C_4B_2 nanosheets presented direct band gaps, in the 1.6−2.0 eV range, being more favorable for optoelectronics applications than C_4N_2 ones, which have indirect band gaps in the 5.4−5.6 eV range.[53] In particular, the small effective masses and high elastic modulus of C_4B_2 systems may contribute to high electron mobility as the mobility formula is given by[20]

$$\mu = \frac{e\hbar^3 C_{11}}{k_B T E_1^2 (m^*)^2} \tag{5}$$

Here, k_B is the Boltzmann constant, E_1 is the deformation potential constant, and T is the temperature. These properties make C_4B_2 systems potentially suitable for applications in photovoltaic cells. However, confirmation necessitates a comprehensive analysis of the optical properties of the C_4B_2 nanosheets. Table 4 summarizes their properties and their respective potential applications.

CONCLUSIONS

In conclusion, we performed an ab initio investigation on the structural, thermodynamic, dynamic, elastic, and electronic properties of the C_4X_2 (X = B or N) systems. According to AIMD simulations, phonon calculations, and the Born stability criteria, all the nanosheets are thermodynamically, dynamically, and mechanically stable. Furthermore, the systems presented standard enthalpy of formation close to the recently synthesized PD composed of three graphene layers. Elastic properties indicated that these nanosheets possess high Young's modulus values and characteristics of isotropic systems. The estimated longitudinal and transversal acoustic velocities revealed that their stiffness is comparable to that of bulk diamond. Finally, the electronic properties of the nanosheets showed some differences. C_4N_2 structures exhibited wide indirect band gaps and heavier effective masses, while the C_4B_2 structures had narrow direct band gaps and lighter effective masses. These results offer chemical pathways to tune the electronic properties of 2D diamonds through doping for specific applications, such as optoelectronic devices.

https://doi.org/10.1021/acsaelm.3c01398
ACS Appl. Electron. Mater. 2024, 6, 386−393

AUTHOR INFORMATION

Corresponding Author

Bruno Ipaves − *Instituto de Física, Universidade de São Paulo, São Paulo CEP 05508-090, São Paulo, Brazil;* orcid.org/0000-0003-2908-4589; Email: ipavesbruno@if.usp.br

Authors

João F. Justo − *Escola Politécnica, Universidade de São Paulo, São Paulo CEP 05508-010, São Paulo, Brazil;* orcid.org/0000-0003-1948-7835

Biplab Sanyal − *Department of Physics and Astronomy, Uppsala University, 75120 Uppsala, Sweden;* orcid.org/0000-0002-3687-4223

Lucy V. C. Assali − *Instituto de Física, Universidade de São Paulo, São Paulo CEP 05508-090, São Paulo, Brazil*

Complete contact information is available at: https://pubs.acs.org/10.1021/acsaelm.3c01398

Notes

The authors declare no competing financial interest.

ACKNOWLEDGMENTS

Brazilian Federal Government Agencies CNPq (grants 314884/2021-1, 302800/2022-0, and 150595/2023-9), CAPES (grants 88882.332907/2019-01 and 88887.371193/2019-00), and FAPESP (grant 2022/10095-8) partially supported this investigation. The authors acknowledge the National Laboratory for Scientific Computing (LNCC/MCTI, Brazil) for providing HPC resources of the Santos Dumont supercomputer, Centro Nacional de Processamento de Alto Desempenho em São Paulo (CENAPAD-SP, Brazil), and SNIC-UPPMAX, SNIC-HPC2N, and SNIC-NSC centers under the Swedish National Infrastructure for Computing (SNIC) resources.

REFERENCES

(1) Novoselov, K. S.; Geim, A. K.; Morozov, S. V.; Jiang, D.; Zhang, Y.; Dubonos, S. V.; Grigorieva, I. V.; Firsov, A. A. Electric field effect in atomically thin carbon films. *Science* **2004**, *306*, 666−669.

(2) Geim, A. K.; Novoselov, K. S. The rise of graphene. *Nat. Mater.* **2007**, *6*, 183−191.

(3) Gao, Y.; Cao, T.; Cellini, F.; Berger, C.; De Heer, W. A.; Tosatti, E.; Riedo, E.; Bongiorno, A. Ultrahard carbon film from epitaxial two-layer graphene. *Nat. Nanotechnol.* **2018**, *13*, 133−138.

(4) Sorokin, P. B.; Yakobson, B. I. Two-Dimensional diamond—diamane: current state and further prospects. *Nano Lett.* **2021**, *21*, 5475−5484.

(5) Qin, G.; Wu, L.; Gou, H. Diamane: design, synthesis, properties, and challenges. *Funct. Diam.* **2021**, *1*, 83−92.

(6) Piazza, F.; Gough, K.; Monthioux, M.; Puech, P.; Gerber, I.; Wiens, R.; Paredes, G.; Ozoria, C. Low temperature, pressureless sp^2 to sp^3 transformation of ultrathin, crystalline carbon films. *Carbon* **2019**, *145*, 10−22.

(7) Grayfer, E. D.; Makotchenko, V. G.; Kibis, L. S.; Boronin, A. I.; Pazhetnov, E. M.; Zaikovskii, V. I.; Fedorov, V. E. Synthesis, properties, and dispersion of few-Layer graphene fluoride. *Chem.—Asian J.* **2013**, *8*, 2015−2022.

(8) Erohin, S. V.; Ruan, Q.; Sorokin, P. B.; Yakobson, B. I. Nano-Thermodynamics of Chemically Induced Graphene−Diamond Transformation. *Small* **2020**, *16*, 2004782.

(9) Ke, F.; Zhang, L.; Chen, Y.; Yin, K.; Wang, C.; Tzeng, Y.-K.; Lin, Y.; Dong, H.; Liu, Z.; Tse, J. S.; Mao, W. L.; Wu, J.; et al. Synthesis of atomically thin hexagonal diamond with compression. *Nano Lett.* **2020**, *20*, 5916−5921.

(10) Kvashnin, A. G.; Chernozatonskii, L. A.; Yakobson, B. I.; Sorokin, P. B. Phase diagram of quasi-two-dimensional carbon, from graphene to diamond. *Nano Lett.* **2014**, *14*, 676−681.

(11) Pakornchote, T.; Ektarawong, A.; Busayaporn, W.; Pinsook, U.; Bovornratanaraks, T. Roles of nitrogen substitution and surface reconstruction in stabilizing nonpassivated single-layer diamond. *Phys. Rev. B* **2020**, *102*, 075418.

(12) Ipaves, B.; Justo, J. F.; Assali, L. V. C. Carbon-Related Bilayers: Nanoscale Building Blocks for Self-Assembly Nanomanufacturing. *J. Phys. Chem. C* **2019**, *123*, 23195−23204.

(13) He, C.; Zhang, M.; Li, T.; Zhang, W. Electric field-modulated high sensitivity and selectivity for NH_3 on α-C_2N_2 nanosheet: Insights from DFT calculations. *Appl. Surf. Sci.* **2020**, *505*, 144619.

(14) Tan, L.; Nie, C.; Ao, Z.; Sun, H.; An, T.; Wang, S. Novel two-dimensional crystalline carbon nitrides beyond gC_3N_4: structure and applications. *J. Mater. Chem. A* **2021**, *9*, 17−33.

(15) Niu, C.; Zhang, J.; Zhang, H.; Zhao, J.; Xia, W.; Zeng, Z.; Wang, X. Configuration stability and electronic properties of diamane with boron and nitrogen dopants. *Phys. Rev. B* **2022**, *105*, 174106.

(16) Niu, C.; Cheng, Y.; Yang, K.; Zhang, J.; Zhang, H.; Zeng, Z.; Wang, X. Boron-dopant enhanced stability of diamane with tunable band gap. *J. Phys.: Condens. Matter* **2020**, *32*, 135503.

(17) Fyta, M. Nitrogen-vacancy centers and dopants in ultrathin diamond films: electronic structure. *J. Phys. Chem. C* **2013**, *117*, 21376−21381.

(18) Zhu, L.; Zhang, T. Suppressed thermal conductivity in fluorinated diamane: optical phonon dominant thermal transport. *Appl. Phys. Lett.* **2019**, *115*, 151904.

(19) Cellini, F.; Lavini, F.; Cao, T.; de Heer, W.; Berger, C.; Bongiorno, A.; Riedo, E. Epitaxial two-layer graphene under pressure: diamene stiffer than diamond. *FlatChem* **2018**, *10*, 8−13.

(20) Cheng, T.; Liu, Z.; Liu, Z. High elastic moduli, controllable bandgap and extraordinary carrier mobility in single-layer diamond. *J. Mater. Chem. C* **2020**, *8*, 13819−13826.

(21) Hohenberg, P.; Kohn, W. Inhomogeneous electron gas. *Phys. rev.* **1964**, *136* (3B), B864.

(22) Kohn, W.; Sham, L. J. Self-consistent equations including exchange and correlation effects. *Phys. Rev.* **1965**, *140*, A1133−A1138.

(23) Kresse, G.; Joubert, D. From ultrasoft pseudopotentials to the projector augmented-wave method. *Phys. Rev. B: Condens. Matter Mater. Phys.* **1999**, *59*, 1758−1775.

(24) Giannozzi, P.; Baroni, S.; Bonini, N.; Calandra, M.; Car, R.; Cavazzoni, C.; Ceresoli, D.; Chiarotti, G. L.; Cococcioni, M.; Dabo, I.; Dal Corso, A.; de Gironcoli, S.; Fabris, S.; Fratesi, G.; Gebauer, R.; Gerstmann, U.; Gougoussis, C.; Kokalj, A.; Lazzeri, M.; Martin-Samos, L.; Marzari, N.; Mauri, F.; Mazzarello, R.; Paolini, S.; Pasquarello, A.; Paulatto, L.; Sbraccia, C.; Scandolo, S.; Sclauzero, G.; Seitsonen, A. P.; Smogunov, A.; Umari, P.; Wentzcovitch, R. M. QUANTUM ESPRESSO: a modular and open-source software project for quantum simulations of materials. *J. Phys.: Condens. Matter* **2009**, *21*, 395502.

(25) Giannozzi, P.; Andreussi, O.; Brumme, T.; Bunau, O.; Buongiorno Nardelli, M.; Calandra, M.; Car, R.; Cavazzoni, C.; Ceresoli, D.; Cococcioni, M.; Colonna, N.; Carnimeo, I.; Dal Corso, A.; de Gironcoli, S.; Delugas, P.; DiStasio, R. A.; Ferretti, A.; Floris, A.; Fratesi, G.; Fugallo, G.; Gebauer, R.; Gerstmann, U.; Giustino, F.; Gorni, T.; Jia, J.; Kawamura, M.; Ko, H.-Y.; Kokalj, A.; Küçükbenli, E.; Lazzeri, M.; Marsili, M.; Marzari, N.; Mauri, F.; Nguyen, N. L.; Nguyen, H.-V.; Otero-de-la-Roza, A.; Paulatto, L.; Poncé, S.; Rocca, D.; Sabatini, R.; Santra, B.; Schlipf, M.; Seitsonen, A. P.; Smogunov, A.; Timrov, I.; Thonhauser, T.; Umari, P.; Vast, N.; Wu, X.; Baroni, S. Advanced capabilities for materials modelling with Quantum ESPRESSO. *J. Phys.: Condens. Matter* **2017**, *29*, 465901.

(26) Perdew, J. P.; Burke, K.; Ernzerhof, M. Generalized gradient approximation made simple. *Phys. Rev. Lett.* **1996**, *77*, 3865−3868.

(27) Dion, M.; Rydberg, H.; Schröder, E.; Langreth, D. C.; Lundqvist, B. I. Van der Waals density functional for general geometries. *Phys. Rev. Lett.* **2004**, *92*, 246401.

(28) Klimeš, J.; Bowler, D. R.; Michaelides, A. Chemical accuracy for the van der Waals density functional. *J. Phys.: Condens. Matter* **2010**, *22*, 022201.
(29) Heyd, J.; Scuseria, G. E.; Ernzerhof, M. Hybrid functionals based on a screened Coulomb potential. *J. Chem. Phys.* **2003**, *118*, 8207−8215.
(30) Monkhorst, H. J.; Pack, J. D. Special points for Brillouin-zone integrations. *Phys. Rev. B: Solid State* **1976**, *13*, 5188−5192.
(31) Baroni, S.; De Gironcoli, S.; Dal Corso, A.; Giannozzi, P. Phonons and related crystal properties from density-functional perturbation theory. *Rev. Mod. Phys.* **2001**, *73*, 515−562.
(32) Garcia, J. C.; de Lima, D. B.; Assali, L. V. C.; Justo, J. F. Group IV graphene- and graphane-like nanosheets. *J. Phys. Chem. C* **2011**, *115*, 13242−13246.
(33) Ipaves, B.; Justo, J. F.; Assali, L. V. Aluminum functionalized few-layer silicene as anode material for alkali metal ion batteries. *Mol. Syst. Des. Eng.* **2023**, *8*, 379−387.
(34) Cadelano, E.; Palla, P. L.; Giordano, S.; Colombo, L. Elastic properties of hydrogenated graphene. *Phys. Rev. B: Condens. Matter Mater. Phys.* **2010**, *82*, 235414.
(35) Ipaves, B.; Justo, J. F.; V C Assali, L. Functionalized few-layer silicene nanosheets: stability, elastic, structural, and electronic properties. *Phys. Chem. Chem. Phys.* **2022**, *24*, 8705−8715.
(36) Larico, R.; Assali, L. V. C.; Machado, W. V. M.; Justo, J. F. Isolated nickel impurities in diamond: A microscopic model for the electrically active centers. *Appl. Phys. Lett.* **2004**, *84*, 720−722.
(37) Assali, L. V. C.; Machado, W. V. M.; Justo, J. F. Manganese impurities in boron nitride. *Appl. Phys. Lett.* **2006**, *89*, 072102.
(38) Assali, L. V. C.; Machado, W. V. M.; Justo, J. F. 3d transition metal impurities in diamond: electronic properties and chemical trends. *Phys. Rev. B: Condens. Matter Mater. Phys.* **2011**, *84*, 155205.
(39) Haastrup, S.; Strange, M.; Pandey, M.; Deilmann, T.; Schmidt, P. S.; Hinsche, N. F.; Gjerding, M. N.; Torelli, D.; Larsen, P. M.; Riis-Jensen, A. C.; Gath, J.; Jacobsen, K. W.; Jørgen Mortensen, J.; Olsen, T.; Thygesen, K. S. The computational 2D materials database: high-throughput modeling and discovery of atomically thin crystals. *2D Mater.* **2018**, *5*, 042002.
(40) Marcondes, M. L.; Santos, S. S. M.; Miranda, I. P.; Rocha-Rodrigues, P.; Assali, L. V. C.; Lopes, A. M. L.; Araújo, J. P.; Petrilli, H. M. On the stability of calcium and cadmium based Ruddlesden−Popper and double perovskite structures. *J. Mater. Chem. C* **2021**, *9*, 15074−15082.
(41) Kresse, G.; Furthmüller, J. Efficient iterative schemes for ab initio total-energy calculations using a plane-wave basis set. *Phys. Rev. B: Condens. Matter Mater. Phys.* **1996**, *54*, 11169−11186.
(42) Pakornchote, T.; Ektarawong, A.; Alling, B.; Pinsook, U.; Tancharakorn, S.; Busayaporn, W.; Bovornratanaraks, T. Phase stabilities and vibrational analysis of hydrogenated diamondized bilayer graphenes: A first principles investigation. *Carbon* **2019**, *146*, 468−475.
(43) Mouhat, F.; Coudert, F.-X. Necessary and sufficient elastic stability conditions in various crystal systems. *Phys. Rev. B: Condens. Matter Mater. Phys.* **2014**, *90*, 224104.
(44) Lee, C.; Wei, X.; Kysar, J. W.; Hone, J. Measurement of the elastic properties and intrinsic strength of monolayer graphene. *Science* **2008**, *321*, 385−388.
(45) Chernozatonskii, L. A.; Sorokin, P. B.; Kuzubov, A. A.; Sorokin, B. P.; Kvashnin, A. G.; Kvashnin, D. G.; Avramov, P. V.; Yakobson, B. I. Influence of size effect on the electronic and elastic properties of diamond films with nanometer thickness. *J. Phys. Chem. C* **2011**, *115*, 132−136.
(46) Kvashnin, A.; Avramov, P.; Kvashnin, D.; Chernozatonskii, L.; Sorokin, P. Features of electronic, mechanical, and electromechanical properties of fluorinated diamond films of nanometer thickness. *J. Phys. Chem. C* **2017**, *121*, 28484−28489.
(47) Gercek, H. Poisson's ratio values for rocks. *Int. J. Rock Mech. Min. Sci.* **2007**, *44*, 1−13.
(48) Hess, P. Bonding, structure, and mechanical stability of 2D materials: the predictive power of the periodic table. *Nanoscale Horiz.* **2021**, *6*, 856−892.
(49) Green, M. A. Intrinsic concentration, effective densities of states, and effective mass in silicon. *J. Appl. Phys.* **1990**, *67*, 2944−2954.
(50) Wickramaratne, D.; Zahid, F.; Lake, R. K. Electronic and thermoelectric properties of van der Waals materials with ring-shaped valence bands. *J. Appl. Phys.* **2015**, *118*, 075101.
(51) Novoselov, K. S.; Mishchenko, A.; Carvalho, A.; Castro Neto, A. H. 2D materials and van der Waals heterostructures. *Science* **2016**, *353*, aac9439.
(52) Garcia, J. C.; Justo, J. F.; Machado, W. V. M.; Assali, L. V. C. Functionalized adamantane: building blocks for nanostructure self-assembly. *Phys. Rev. B: Condens. Matter Mater. Phys.* **2009**, *80*, 125421.
(53) Chaves, A.; Azadani, J. G.; Alsalman, H.; Da Costa, D.; Frisenda, R.; Chaves, A.; Song, S. H.; Kim, Y. D.; He, D.; Zhou, J.; Castellanos-Gomez, A.; Peeters, F. M.; Liu, Z.; Hinkle, C. L.; Oh, S.-H.; Ye, P. D.; Koester, S. J.; Lee, Y. H.; Avouris, P.; Wang, X.; Low, T. Bandgap engineering of two-dimensional semiconductor materials. *npj 2D Mater. Appl.* **2020**, *4*, 29.

https://doi.org/10.1021/acsaelm.3c01398
ACS Appl. Electron. Mater. 2024, 6, 386−393